

Kinetics and Mechanisms of Protein Crystallization at the Molecular Level

Peter G. Vekilov

Summary

This chapter focuses on the processes by which a protein molecule in a supersaturated solution joins a protein crystal. The pair of proteins ferritin/apoferritin is used as an example. The most commonly used technique in such investigations has been atomic force microscopy. I discuss the modifications and tests of the atomic force microscope necessary to obtain real-time, *in situ* molecular resolution imaging. Then, I review tests that establish a quantitative correspondence between the continuous models of crystal growth and the discrete nature of the processes at the molecular level. I address the issue of whether the incorporation of a molecule from a solution into a growth site on the crystal surface is limited by the slow rate of decay of an Eyring-type transition state. The conclusion is that, on the contrary, a scenario, envisioned by Smoluchowski and Debye, is followed in which the kinetics is only limited by the rate diffusion over the free-energy barrier of interaction between two molecules, or an incoming molecule and a surface. Review of the data for many other protein and nonprotein systems suggests that this conclusion is valid not only for the crystallization of ferritin/apoferritin, but also for many other protein and small-molecule crystallization systems. Finally, I review results establishing that the pathway that a molecule from a solution takes on its way to an incorporation site on the crystal surface is indirect: it includes adsorption on the surface and two-dimensional diffusion toward the incorporation site. These results will likely contribute to the understanding at the molecular level not only of the processes of crystallization of proteins and small molecules, but also of the deposition of layers of proteins and other soft materials on substrates, and of other processes of self-assembly in solution.

Key Words: Crystallization; solution thermodynamics; atomic force microscopy; diffusion-limited kinetics; transition states; activation energy; growth mechanisms; surface diffusion; direct incorporation.

From: *Methods in Molecular Biology*, vol. 300:
Protein Nanotechnology, Protocols, Instrumentation, and Applications
Edited by: T. Vo-Dinh © Humana Press Inc., Totowa, NJ

1. Introduction

Crystallization of proteins, as any other phase transition, occurs through a combination of processes at molecular, mesoscopic, and macroscopic length scales. During phase transitions in solution, molecular-level phenomena include the interactions between the molecules that alter the free energy landscape to cause the formation of the new phase and determine the driving force for the phase transformation; attachment of molecules to the new phase during growth; formation of sites suitable for molecular attachment; and generation of defects. On the mesoscopic length scale, one could consider the nucleation of droplets, clusters, or crystallites of the new phase; generation of new layers of a crystal controlled by capillarity; and interactions between growth steps as they propagate along the crystal's surfaces. Macroscopic length scales govern the fluxes of energy and mass through the interface (i.e., the transport of building blocks to the growing phase and the dissipation of heat away from it), as well as the balance and distribution of stress and strain in a solid and the transition from elastic to plastic deformations.

In this chapter, I focus on the molecular-level processes during the growth of crystals of the pair of proteins ferritin and apoferritin. Ferritin is the main nonheme iron storage protein in cytosol (1–3). The protein shell consists of 24 subunits, arranged in pairs along the 12 facets of a rhombododecahedron (4,5). Ferritins have been extensively studied as an example of biological mineralization occurring *in vivo* (6,7). The iron-containing core of ferritin can be replaced with other organic, inorganic, and bioorganic compounds for potential applications in the areas of nanoassembly, drug delivery, biomineralization, and so on (8,9). Apoferritin is the protein shell from which the ferrite core has been removed by dissolution into an acidic solution. The structures of the proteins from various species are known down to 1.90 Å resolution (5).

In the presence of Cd^{2+} , ferritin and apoferritin crystallize in the cubic F432 group (3,5). Contrary to typical protein crystallization cases, in which the electrolyte serves to screen the repulsion between the similarly charged protein molecules, in the case of apoferritin, Cd^{2+} is involved in specific bonds between the molecules (5). This specificity makes the case of apoferritin crystallization a relevant first-approximation model of other self-assembling systems, such as *vir*i, protein complexes, and nanoparticles.

The crystals, such as the one in **Fig. 1**, are typically faceted by octahedral (111) faces pierced by the threefold axis belonging to the symmetry group. The highly symmetric shape of the ferritin and apoferritin molecules makes the approximation of isotropic molecular shape realistic. In addition, the symmetry of the environment of a molecule in a crystal makes quantitative insight easier to obtain and comprehend. Because of these two factors, ferritin and apoferritin crystallization is a particularly appealing system for in-depth investigations of the thermodynamics and kinetics of phase transitions.

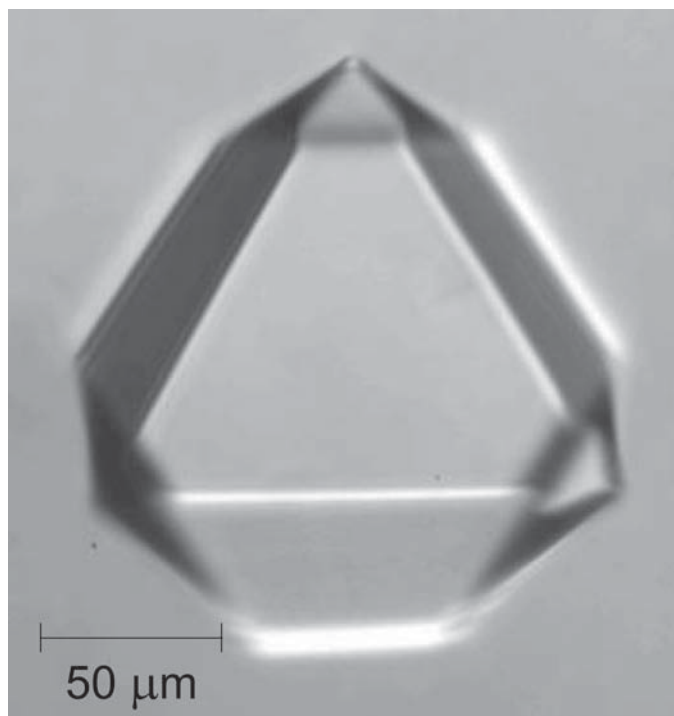


Fig. 1. Typical octahedral crystal of apoferritin, resting on cell bottom with a (111) face facing upward. Ferritin crystals appear identical except for the ruby red color.

In this chapter, I first define the methods used to characterize the growth kinetics on the molecular length scale. Then, I discuss tests of the correspondence between discrete approaches to the kinetics of attachment, in which the growth rate and other spatial and temporal characteristics of the growth process are represented as a statistical averages of events involving individual atoms or molecules, and continuous approaches, in which fluxes of matter toward the growth interface are evaluated. Finally, I show that the kinetics of incorporation of the molecules into growth sites on the surface of a crystal are not determined by decay of a high-energy transition state but are only limited by the diffusion of the incoming molecule over a barrier owing to the hydration shells around incoming molecules.

2. Methods

2.1. Atomic Force Microscopy

In our laboratory, we used Nanoscope IIIa or Nanoscope IV Multimode atomic force microscopes from Digital Instruments, equipped with a 120- μm ("J")

scanner and a Tapping Mode fluid cell. The preparation of crystals and solutions and the cell loading are very similar to those used in numerous other investigations and are discussed in detail in **ref. 10**.

Temperature in the laboratory was stabilized to approx $22 \pm 0.5^\circ\text{C}$. To control the temperature in the crystallization solution, we mounted the sample onto a Peltier-cooled disk firmly attached to the scanner. This allowed imaging in the range of 28 to 45°C ; to access 25 and 20°C , the room temperature was set at 18 to 20°C . Temperature in the fluid cell was monitored with a thermocouple imbedded into the metal disk under the solution droplet and was found to be steady within 0.1°C .

All images were collected *in situ* during growth of the crystals using the less intrusive tapping-imaging mode (**11,12**). This allows visualization of adsorbed protein and impurity species (tip impact in the contact-imaging mode often prevents such imaging).

We used standard SiN tips and tapping drive frequency was adjusted in the range of 25 to 31 kHz to the resonance value for the specific tip used. Other scanning parameters were adjusted such that continuous imaging affected neither the surface structure nor the process dynamics. For verification, we varied the scan sizes and the time elapsed between image collections and saw that neither the spatial nor the temporal characteristics of the processes changed.

2.2. Atomic Force Microscopy Data

We employed three types of atomic force microscopy (AFM) data collection. The first type consisted of images of 200 nm to 1 mm, such as the one in **Fig. 2**, on which the protein molecules, 13 nm in size were clearly detectable. Calibration of the microscope was verified by determining the spacing of molecules along a densely, packed direction in the lattice and the thickness of the top crystalline layer. As **Fig. 2** reveals, the respective numbers for one of the systems, used for the studies summarized here, the protein apoferritin, are 13.1 and 10.5 Å. These are in good agreement with the evaluations from the X-ray structure of the crystal. Using the crystal lattice parameter of $a = 18.4$ nm for the crystallographic group F432 (**4,5**), the intermolecular spacing is $(1/2)(2a^2)^{1/2} = 13.0$ nm, and the layer thickness is $(1/3)(3a^2)^{1/2} = 10.6$ nm.

To evaluate the maximum resolution of molecular-scale imaging attainable with ferritin/apoferritin *in situ*, during crystallization, we scanned a 200×200 nm square on the surface of a ferritin crystal (*see Fig. 3A*). The two-dimensional Fourier transform of the image in **Fig. 3B** has the expected hexagonal symmetry, with the distance between the peaks in the first hexagon and the center of the plot corresponding to resolution equal to the molecular size of 13 nm. The maximum resolution, determined from the location of the most distant

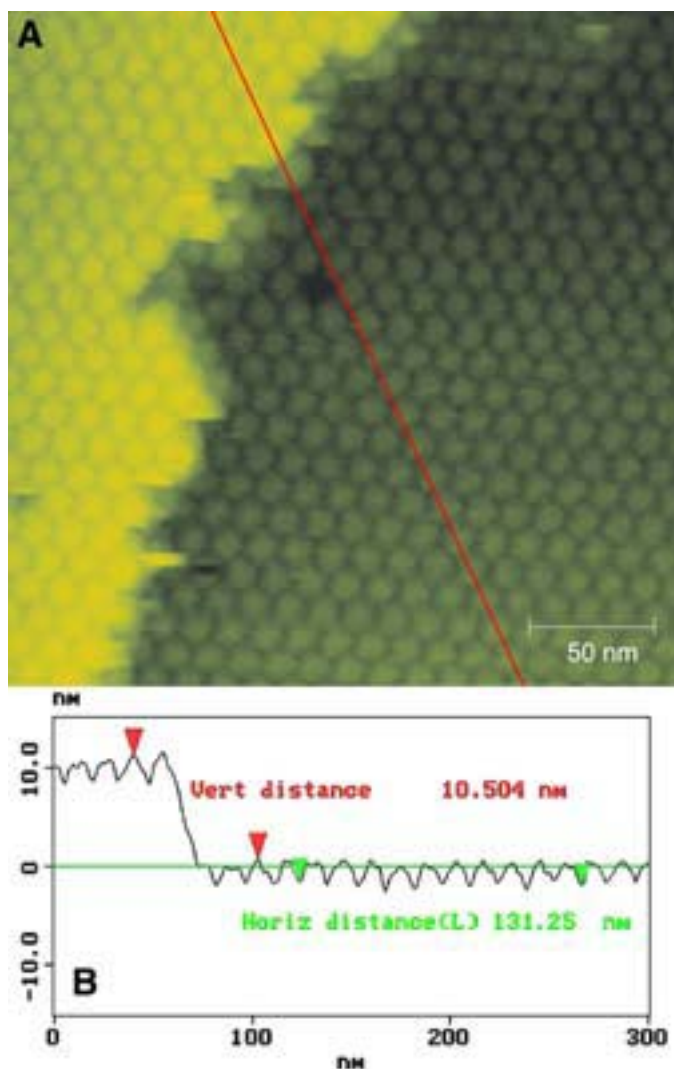


Fig. 2. Accuracy of AFM imaging. (A) View of a (111) apoferritin crystal face; (B) height profile along line in (A) allowing determination of layer thickness and molecular spacing. (From **ref. 10.**)

peak, is 1.6 nm. This resolution allows us to distinguish some of the submolecular-level details of the molecules on the crystal surface in **Fig. 3C**. Comparison with the structure of the molecules coming from an X-ray determination in **Fig. 3D (5)** shows that the triangular formation in **Fig. 3C** likely corresponds to bundles of α -helices.

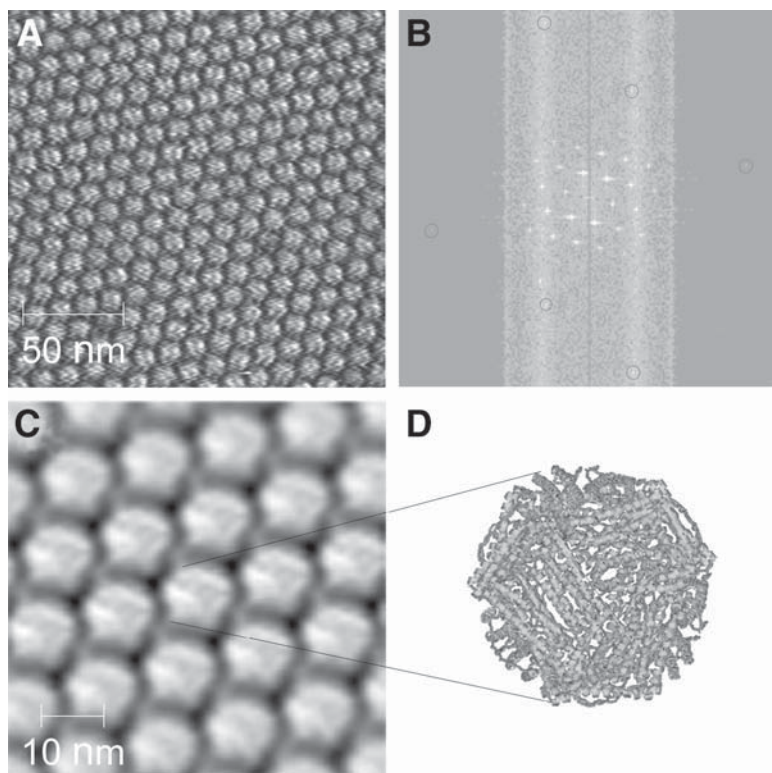


Fig. 3. Resolution of AFM imaging. **(A)** Real-space high-resolution image of a (111) apoferritin crystal face. (From **ref. 10.**) **(B)** Fourier transform of A: circles highlight high-resolution peaks; eighth-order peaks at the top and bottom of the image correspond to a resolution of approx 1.6 nm. (From **ref. 10.**) **(C)** Real-space image in which each molecule is replaced by average of all molecules in frame; processed with SEMPER Software package (N. Braun, S. Weinkauff, personal communication). **(D)** Ribbon presentation of X-ray structure of apoferritin molecule viewed along (111) direction. Images of molecules in C appear to have similar triangular features.

The second type of AFM data consisted of images on the mesoscopic length scales from several tens of nanometers to several micrometers, as in many previous AFM studies of crystallization from solution (**13–24**). These images, similar to the one in **Fig. 4**, with a view-field width between 2 and 40 μm , allow characterization of growth steps and step patterns.

For the third type of AFM data, we employed scans with a disabled y-axis (**25,26**), as in previous scanning tunneling microscopy (STM) work on metals and semiconductors in ultrahigh vacuum (**27–30**). The AFM tip is drawn over a single line of the crystal surface. In the collected pseudoimages, the vertical

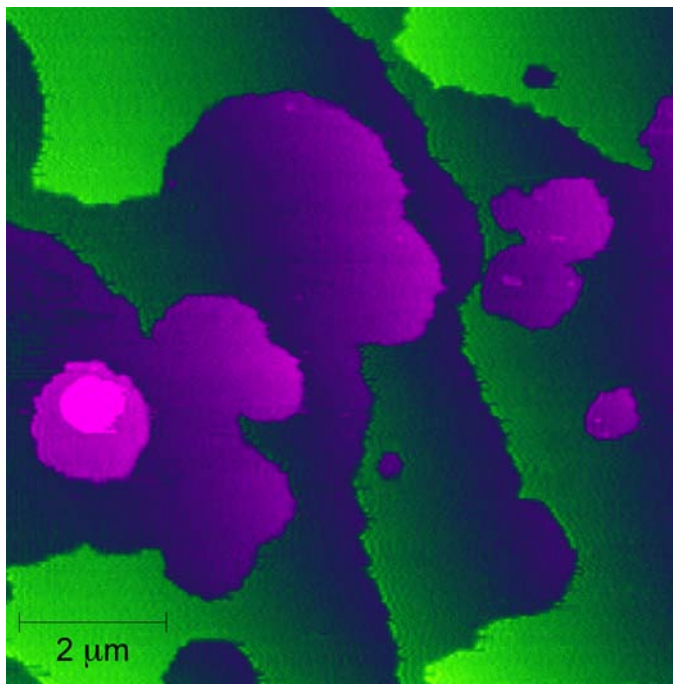


Fig. 4. AFM images of surface of growing apoferritin crystals taken near center of respective facet. Facet size is approx 90 μm , ensuring near-uniform supersaturation over the facet. New crystal layers are generated at random locations by surface nucleation and spread to merge with other islands and cover the whole facet.

axis represents time. The technique allows monitoring of processes with characteristic times of fractions of a second.

If the scan widths were 600 nm and less, the displacement of a single site on the step could be monitored with molecular resolution; that is, we could trace the attachment and detachment of single molecules to and from steps (*10,25,31*). Data collection lasted typically 2 to 3 min. Immediately after such scans, area scans included the line along which the tip was drawn. In about 80% of cases, these tests revealed that the tip impacted over the same location had delayed the growth. These data were discarded, and only data sets that did not show tip impact are discussed herein.

2.3. Determination of Step Velocities

During growth of crystals by the generation and spreading of layers, the rate of growth of the newly formed layers, often called step velocity, is the main kinetic variable, and its link to the driving force determines the main kinetic

parameter, the step kinetic coefficient. In the studies discussed here, we employed three methods of step velocity determination.

As a first method, we used sequences of molecular resolution *in situ* AFM images of the advancing steps, as in **Fig. 2**. The step velocities were determined as the ratio $Na/\Delta t$, in which N is the number of molecular sizes a that the step advances for the time between two sequential images Δt . For each concentration of ferritin or apoferritin, approx 20 determinations of v were done and averaged (32). This method is applicable to step velocities $<5 \text{ nm s}^{-1}$, at which a step would advance by several molecular sizes for the time required for image collection, approx 1 min (10,25).

For step velocity data at higher driving forces, we disabled the slow scanning axis of the AFM (25). This allowed us to monitor for times of 60 to 90 min with a frequency of 2 to 4 s^{-1} the propagation of 15 to 30 steps within 10- μm segments of a growing crystal surface (26).

To ensure the veracity of the kinetics data, we crosschecked the results of the AFM determinations with interferometry. This method is applicable to step velocities as fast as 100 nm/s. We extracted averaged values of the step velocities from time traces of this variable recorded with a frequency of 1 s^{-1} at chosen points on the growing crystal surface using laser interferometry. Each point represents the average of approx 1000 measurements (33,34); the data scatter intervals were evaluated as 90% confidence interval for this average (32). Complete details about this method are provided in refs. 34–36.

3. Characterization of Test System

3.1. Molecular Mass, Size, and Intermolecular Interactions

The molecular mass of apoferritin has been determined by many techniques to be $M_w = 450,000 \text{ g/mol}$ (2,3), with the mass of a molecule $m = 7.47 \times 10^{-19} \text{ g}$. However, the average M_w of ferritin varies between 550,000 and 950,000 g/mol, depending on the size of the ferrite core (2,3). To determine the M_w of ferritin in the samples used here, we performed static light scattering (37) in 0.05 M NaOOCCH_3 solutions. The molecular masses M_w and the second osmotic virial coefficients A_2 in dimensional form were determined from the Debye plots, $(KC/R_0) = [(1/M_w) + 2A_2C]$, in **Fig. 5**, in which R_0 is the Raleigh ratio of the scattered to the incident light intensity; K is a system constant, $K = (1/N_A) (2\pi n_0/\lambda^2)^2 (dn/dC)^2$; $n_0 = 1.3320$ is the refractive index of the solvent at the wavelength of the laser beam $\lambda = 0.6328 \text{ mm}$ (38,39); and dn/dC is the n -increment with the protein concentration C , determined for each protein at $\lambda = 0.628 \text{ mm}$ by a differential refractometer—for ferritin $dn/dC = 0.290 \text{ cm}^3/\text{g}$, and for apoferritin, $dn/dC = 0.159 \text{ cm}^3/\text{g}$.

The Debye plots in **Fig. 5** show that for ferritin, $M_w = 780,000 \text{ g/mol}$, $m = 1.30 \times 10^{-18} \text{ g}$, and, as expected, for apoferritin, $M_w = 450,000 \text{ g/mol}$.

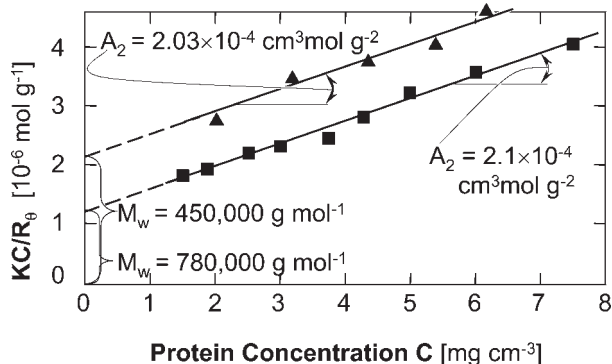


Fig. 5. Static light-scattering characterization of ferritin (■) and apoferritin (▲) molecules in 0.05 *M* NaOOCCH₃ solutions. The Debye plots are $(KC/R_0) = [(1/M_w) + 2A_2C]$ (R_0 is the Raleigh ratio of the scattered to the incident light intensity, K is a system constant, and C is protein concentration in mg/mL). The molecular masses, M_w , and the second osmotic virial coefficients in the dimensional form, A_2 , of the two proteins are shown in the plot. The repulsion between the protein molecules (37,82) ensures nonaggregating sample of well-separated monomers. (From ref. 40.)

Figure 5 also shows that values of the second osmotic virial coefficients, A_2 , for the two proteins are similar. This is not surprising since A_2 characterizes the pair interactions between the solute molecules, determined by the identical surfaces of the molecules.

As expected, the size distributions of the scatterers in solutions of the two proteins resulting from a dynamic light-scattering determination (37) are narrow, and the two proteins have identical diameters of 13 nm (40). This is equal to their identical crystallographic diameters (2–4). Since these sizes are calculated from the set of experimentally determined diffusivities using the Einstein-Stokes law of Brownian motion, the equality to the crystallographic data indicates that the diffusion of both molecules obeys this law (41).

3.2. Solubility and Driving Force for Crystallization

The crystallization driving force is written as

$$\{\exp[-(\mu_c - \mu_s)/k_B T] - 1\} \cong (C/C_e - 1) = (n/n_e - 1) \quad (1)$$

in which

$$\mu_s = \mu_0 + k_B T \ln(\gamma C) \text{ and } \mu_c = \mu_0 + k_B T \ln(\gamma_e C_e) \quad (2)$$

In these expressions, subscripts *c* and *s* denote crystal and solute, respectively; C and n are, respectively, the protein mass and molecular concentrations, $n = C/m$; for determinations of the molecular masses m of ferritin and apoferritin,

see **Subheading 3.1.**; and the subscript e indicates their values at equilibrium with the crystal.

To determine the solubility of ferritin and apoferritin at 27°C, we monitored trains of growth steps and gradually decreased the apoferritin concentration in the solution. We found that at a certain C , the propagation of the steps stopped, and when the concentration was lowered below this value, the step movement was backward, and the crystal was dissolving. The concentration of equilibrium between crystal and solution $C_e = 35 \pm 5$ mg/mL for ferritin, and $C_e = 23 \pm 4$ mg/mL for apoferritin.

Characterization using static light scattering of the solution nonideality in crystallizing solution containing Cd^{2+} in addition to the NaOOCCH_3 (**10**) revealed that the activity coefficients γ were 0.996 in a 100 $\mu\text{g/mL}$ solution of ferritin, and 0.998 in an apoferritin solution of the same concentration, and correspondingly closer to unity at a lower concentration of the proteins.

3.3. Statistical Thermodynamics Arguments of Independence of Solubility on Molecular Mass

The values for n_e , determined as discussed in **Subheading 3.2.** and in **refs. 10,25** for ferritin and apoferritin are, respectively, $(2.7 \pm 0.5) \times 10^{13} \text{ cm}^{-3}$ and $(3.0 \pm 0.5) \times 10^{13} \text{ cm}^{-3}$. They are equal within the error limits, suggesting that the solubilities of these proteins do not depend on their molecular mass. Next, I provide statistical-mechanical arguments that indicate that this may be the case for protein molecules with near-spherical symmetry.

To rationalize the apparently equal solubility of ferritin and apoferritin, we consider the equilibrium between the solution and a crystal. This is equivalent to equilibrium between the states of a molecule in a kink on the crystal surface and in the solution (**42–44**). At constant temperature and pressure, the activity of a molecule in the crystal does not depend on the concentration of the solute and is equal to the activity of the standard crystal state (**45,46**). Then, the equilibrium constant K_{cryst} can be written as

$$K_{\text{cryst}} = (\gamma_e C_e)^{-1} \cong C_e^{-1} \quad (3)$$

in which g_e is the protein activity coefficient at a protein concentration equal to the solubility, and C_e is the solubility. The activity coefficient depends on the protein concentration and on the intermolecular interactions. Hence, we expect equal γ s in solutions of ferritin and apoferritin of equal concentration. As shown in **Subheading 3.2.**, determinations of γ for apoferritin solutions of concentrations up to 20-fold higher than the solubility have yielded $\gamma \cong 1$ (**10**). We expect the same to be true for ferritin, and this is the basis of the second equality in **Eq. 13** above for these two proteins.

From the point of view of statistical thermodynamics, the equilibrium constant for crystallization K_{cryst} can be written as (47)

$$K_{cryst} = q_0 \exp(\mu_0/k_B T) \quad (4)$$

in which q_0 is the partition function of a molecule in a kink (which is only a function of temperature and pressure), and μ_0 is the standard chemical potential of a molecule in the solution.

To evaluate q_0 and μ_0 , we assume that the internal molecular vibrations in the solution are the same as in the crystal and are decoupled from the other degrees of freedom. This allows us to neglect the internal vibrational partition function for both states. Furthermore, we limit ourselves to only translational contributions to the solute partition function, neglecting the rotational contributions, and those stemming from the intermolecular interactions. This limits the validity of the considerations below to molecules similar to the ferritin-apoferritin pair: with symmetry close to spherical, and that only exhibit very weak intermolecular interactions and activity coefficients close to 1.

We do not take into account the contribution of the release or binding of the solvent molecules to the free-energy changes in the phase transition. Although arguments presented in **Subheading 5.2.** indicate that these contributions may be significant (10), we expect the contributions of the solvent effects to be identical for ferritin and apoferritin. This justifies neglecting them while aiming at comparisons between the two proteins. We also neglect the rotational vibrations in the crystal.

With these assumptions, we can use the expressions for the partition functions from **ref. 47**, and write

$$q_0 = q_x q_y q_z \cong (q_{vib})^3 \quad (5)$$

in which q_i ($i = x, y, z$) are the partition functions for translational vibrations along the respective coordinate. In turn, with h the Planck constant, n the vibration frequency, and U the mean-force potential of a molecule in a kink,

$$q_{vib} = \frac{\exp\left(-\frac{h\nu}{k_B T}\right)}{1 - \exp\left(-\frac{h\nu}{k_B T}\right)} \approx \frac{k_B T}{h\nu}, \quad \nu = \frac{1}{2\pi} \sqrt{\frac{f}{m}}, \quad \text{where } f = \left(\frac{\partial^2 U}{\partial t^2}\right)_{\min} \quad (6)$$

Combining, we obtain for q_{vib} and q_0

$$q_{vib} = \frac{2\pi k_B T}{h} \sqrt{\frac{m}{f}}, \quad q_0 = \left(\frac{2\pi k_B T}{h}\right)^3 \left(\frac{m}{f}\right)^{3/2} \quad (7)$$

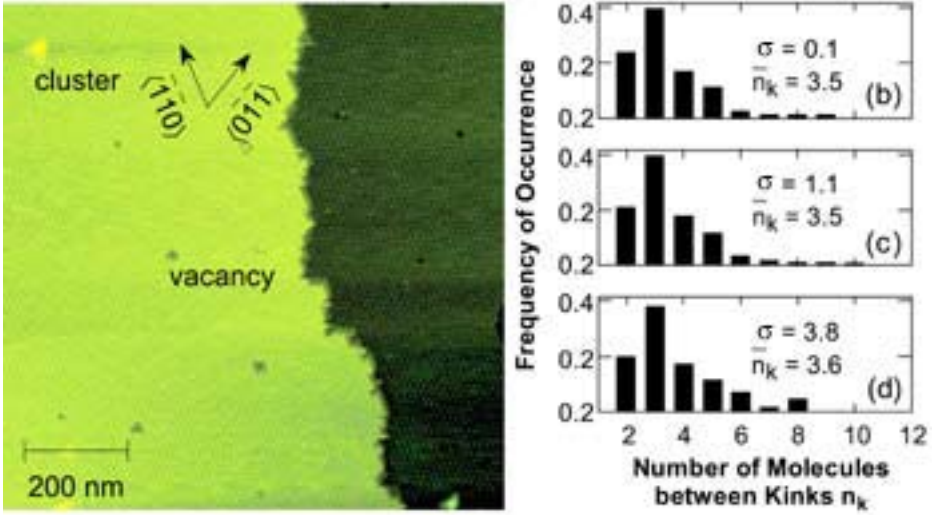


Fig. 6. (A) Molecular structure of growth step on apoferritin crystal at protein concentration of 70 mg/mL, corresponding to supersaturation $\sigma = \Delta\mu/k_B T = 1.1$, $(C/C_e - 1) = 2.04$. Dark area: lower layer; light area: advancing upper layer. Adsorbed impurity clusters and surface vacancies are indicated. (B–D) The distribution of the number of molecules between kinks on steps located $>0.5 \mu\text{m}$ apart, obtained from images similar to **Fig. 1**, at the three supersaturations s indicated in the plots is shown. The mean values of the distributions for each case are also shown. The protein concentrations corresponding to these σ 's are (B) 25 $\mu\text{g/mL}$, (C) 70 $\mu\text{g/mL}$, and (D) 1 $\mu\text{g/mL}$. (From **ref. 10**.)

For m_0 , we have (47)

$$\frac{\mu_0}{k_B T} = -\ln \left[\left(\frac{2\pi m k_B T}{h^2} \right)^{3/2} k_B T \right] \quad \text{and} \quad \exp \left(\frac{\mu_0}{k_B T} \right) = \frac{1}{k_B T} \left(\frac{h^2}{2\pi m k_B T} \right)^{3/2} \quad (8)$$

We see that q_0 contains $m^{3/2}$, while $\exp(\mu_0/k_B T)$ is proportional to $m^{-3/2}$; that is, their product K_{cryst} and C_e do not depend on the mass of the molecule.

4. Growth Sites

4.1. Kinks and Kink Density

Under all conditions used in the experiments reported here, the crystals of ferritin and apoferritin as seen in the optical microscope attached to the atomic force microscope had the typical octahedral shapes with sharp edges. Accordingly, the AFM images in **Fig. 4, 6–9** and all figures below indicate growth by layer generation and spreading to cover the whole facet.

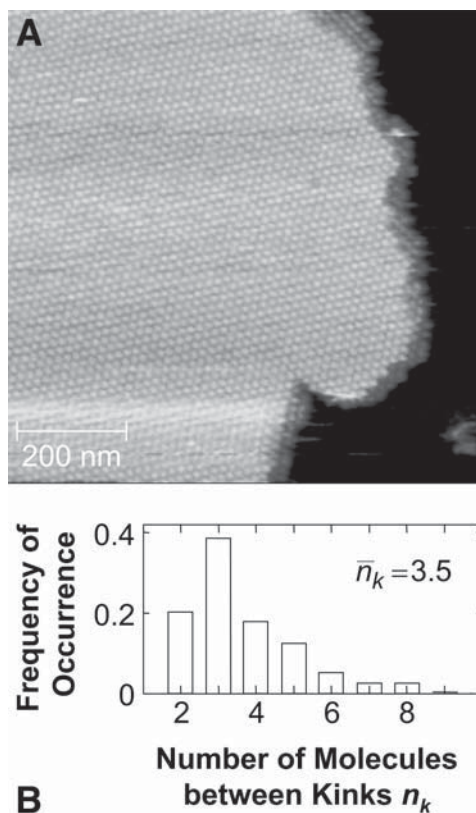


Fig. 7. (A) Molecular structure of growth step on ferritin crystal at protein concentration of 70 mg/mL, corresponding to supersaturation $\sigma = \Delta\mu/k_B T = 0.7$, $(C/C_e - 1) = 1$. Dark area: lower layer; light gray: advancing upper layer. (B) Distribution of molecules between kinks on steps located approx 0.5 mm apart, obtained from images similar to (A) at same $(C/C_e - 1) = 1$. (From ref. 31.)

The molecular structures of a (111) apoferritin face and of a growth step are shown in **Fig. 6**. The kinks at a step are the sites where incoming molecules attach. A molecule attached at a kink has half of the neighbors that a molecule in the crystal bulk has; in the f.c.c. lattice of ferritin and apoferritin, the half-number equals six, with three molecules belonging to the underlying layer, and three molecules from the step (42,43,48). Thus, the kink density is a fundamental variable that determines the ability of the crystal to incorporate solute molecules and grow (49,50).

From **Fig. 6** and approx 15 other similar images, we determine the kink density along a step by counting the molecules between two kinks, n_k , also called kink length (51) and plot their distribution in **Fig. 6B–D** for apoferritin, and in **Fig. 7B** for

ferritin. Note that kink density is affected by the presence of surface point defects, such as vacancies or vacancy clusters, seen in **Fig. 6A**, as well as impurity cluster adsorbed on the surface (37). These features act as stoppers: straight step segments as long as eight molecules form and the step propagation is locally delayed (25). Hence, for the statistics in **Figs. 6** and **7**, we did not consider step segments around such stoppers. We obtain $\bar{n}_k = 3.5$ for both proteins. Comparing **Fig. 6A–C**, we see that the n_k distributions are nearly the same near equilibrium, as well as at very high supersaturations.

4.2. Energy of Kinks and Molecular Interaction Energy

The lack of dependence of the kink density on the thermodynamic supersaturation suggests that the kinks are not created by nucleation of molecular rows along a step; such nucleation would result in a steep dependence of kink density on supersaturation (52,53). Hence, the kink density $1/n_k$ appears to be an equilibrium property of this surface even during growth in a supersaturated environment. In this case, the number of molecules between the kinks n_k is solely determined by the balance of molecular interactions and thermal fluctuations in the top crystal layer (28,29,54,55) and should be a function of the energy w needed to create a kink. Derivations have shown (49) that the average \bar{n}_k

$$\bar{n}_k = \frac{1}{2} \exp(w/k_B T) + 1 \quad (9)$$

From the value of \bar{n}_k in **Figs. 6** and **7**, $w = 1.6 k_B T$. Quite surprisingly, this value of w is only slightly lower than the energy of kinks on Si crystals (30); one would expect the strong covalent bonds in the Si crystal lattice to lead to significantly higher kink energies. For the orthorhombic form of lysozyme, it was found that $w = 7.4 k_B T$ (52). This significantly higher value leads to an extremely low kink density with n_k as high as 400 to 800, and step propagation limited by the rate of kink generation (52).

If we assume only first-neighbor interactions, we can evaluate the intermolecular bond energy, ϕ . When a molecule is moved from within the step on a (111) face of an f.c.c. crystal to a location at the step, four kinks are created. For this, seven bonds (four in the top layer and three with molecules from the underlying layer) are broken, and five are formed. Then, $w = \phi/2$ and $\phi = 3.2 k_B T \cong 7.8 \text{ kJ/mol} = 0.09 \text{ eV}$.

The intermolecular bonds in ferritin and apoferritin crystals involve two chains of bonds $\text{Asp} - \text{Cd}^{2+} - \text{Glu}$ between each pair of adjacent molecules (4,5). The preceding value of ϕ seems significantly lower than the typical coordination bond energies. This low value may stem from the need to balance Cd^{2+} coordination with the amino acid residues and with the water species

(H₂O and OH⁻), or from free-energy loss owing to spatially and energetically unfavorable contacts by the other amino acid residues involved in the intermolecular contacts.

5. Thermodynamics of Crystallization and Crystal Morphology

5.1. Aspects of Macroscopic Thermodynamics

In the search for temperature dependence of the solubility, crystals were grown in the flat cell, allowing good optical microscopic observation. At various stages in the development of the individual crystals, corresponding to crystal sizes between 20 and 400 nm, the temperature was varied between 0 and 40°C. A significantly faster growth rate that would correspond to a higher supersaturation at a lower solubility was not noticed at either the low or the high limits of this temperature range. Furthermore, no rounding of the crystal edges was detected that would indicate crystal dissolution owing to higher solubility. These observations are interpreted as an indication of none or very weak temperature dependence of the solubility (56).

Temperature-independent solubility means that the equilibrium constant of crystallization is also independent of temperature. Hence (57),

$$\left(\frac{\partial \ln K}{\partial T} \right)_p = - \left(\frac{\partial \Delta G^\circ / RT}{\partial T} \right) = \frac{\Delta H^\circ}{RT^2} = 0 \quad (10)$$

in which R is the gas constant, or

$$\left(\frac{\partial \Delta G^\circ}{\partial T} \right) = \frac{\Delta G^\circ}{T} \quad (11)$$

Equation 11 has a simple solution:

$$\Delta G^\circ = \text{const} \times T \quad (12)$$

Using $\Delta G^\circ = \Delta H^\circ - T\Delta S^\circ$, we obtain that $\Delta H^\circ = 0$ and $\Delta S^\circ = \text{const}$.

The lack of temperature dependencies of the solubility leads to the following conclusions: (1) the enthalpy of crystallization is zero (or extremely small), and (2) the entropy of crystallization is temperature independent (or a weak function of temperature).

5.2. Molecular Processes Underlying Enthalpy, Entropy, and Free Energy for Crystallization

The intermolecular bond energy ϕ contains both enthalpy and entropy components. The enthalpy ones are owing to the ion-mediated, hydrogen, and other bonds between the molecules, and the entropy components stem from the net

release or binding of water and other small molecules on crystallization (45). With this in mind, we can write an expression for the free energy for crystallization as follows:

$$\Delta G^\circ = \Delta H^\circ - T\Delta S^\circ_{\text{solvent}} - T\Delta S^\circ_{\text{protein}} \quad (13)$$

Here, $\Delta H^\circ - T\Delta S^\circ_{\text{solvent}}$ are contributions associated with ϕ , and $\Delta S^\circ_{\text{protein}}$ is the loss of entropy of the protein molecules. A crude estimate of $\Delta S^\circ_{\text{protein}}$ and of the relative weights of the two entropy contributions can be obtained by comparing the standard free-energy change for apoferritin crystallization ΔG° determined from the solubility to the value corresponding to the intermolecular bond *free* energy ϕ .

By converting the solubility of the apoferritin (23 mg/mL) to molality, $C_e = 5.2 \times 10^{-8}$ mol/kg. At equilibrium between crystal and solution, for apoferritin

$$\Delta G = G^\circ(\text{crystal}) - [G^\circ(\text{solution}) + N_A k_B T \ln(C_e)] = 0 \quad (14)$$

in which N_A is the Avogadro number, and the product $N_A k_B = R$ is the universal gas constant. Hence,

$$\Delta G^\circ = G^\circ(\text{crystal}) - G^\circ(\text{solution}) = N_A k_B T \ln C_e \quad (15)$$

in which $\Delta G^\circ = -42$ kJ/mol.

To get $\Delta H^\circ - T\Delta S^\circ_{\text{solvent}}$ from $\phi = 3 k_B T \cong 7.3$ kJ/mol, we have to multiply ϕ by $Z_1/2 = 6$, the half-number of neighbors in the crystal lattice (two molecules partake in a bond, in an f.c.c. lattice $Z_1 = 12$) and, accounting for the sign, we get -44 kJ/mol. The closeness of $\Delta H^\circ - T\Delta S^\circ_{\text{solvent}}$ to ΔG° indicates the insignificance of $\Delta S^\circ_{\text{protein}}$ for the free energy of crystallization.

As shown above, the enthalpy of crystallization and the related energy of pair interactions in the solution are close to zero. In combination with the insignificance of $\Delta S^\circ_{\text{protein}}$, this allows us to conclude that crystallization is mostly driven by the maximization of the entropy of the solvent. Such disordering may stem from the release on crystallization of the water and other solvent components bound to the protein molecules in the solution. A similarity can be traced to the processes that underlie hydrophobic attraction, which governs many processes in nature (58), including some stages of protein folding (59).

The standard free energy of formation of a single intermolecular bond in apoferritin crystals is -7.8 kJ/mol (*see Subheading 4.2.*) and is fully attributable to the entropy gain caused by the release of water, $\Delta S^\circ_{\text{solvent}} = 26.6$ J/(mol·K) per intermolecular bond (10).

This conclusion allows us to estimate crudely the number of water molecules n_w released at the contact between two hemoglobin molecules. Following an analogy first put forth by Tanford (60), we compare the entropy effect of Hb crystallization to the entropy change for melting of ice = at 273 K, $\Delta S^\circ_{\text{ice}} =$

22 J/(mol·K) (**45,61,62**). Similarly, estimates of the entropy loss owing to the tying up of hydration water in crystals have yielded 25 to 29 J/(mol·K) (**62**). Using these numbers, the values of $\Delta S^\circ_{\text{solvent}}$ reflect the release of one or two water molecules per intermolecular bond.

This low number of water molecules can be tentatively linked to the structure of the intermolecular bonds in the face-centered cubic apoferritin crystals. The X-ray structure reveals that each of the 12 such bonds consists of a pair of Cd^{2+} ions (**4**). Around each Cd^{2+} ion of the pair, two of the six coordination spots are occupied by an aspartic acid residue from the one apoferritin molecule partaking in the bond and a glutamic acid residue from the other (**5**). The fact that the entropy change corresponds to the release of one or two, rather than four, water molecules suggests that the Cd^{2+} ions may be prebound to either the incoming apoferritin molecule or the apoferritin molecules already in the crystal.

Thus, as suggested by the crystal structures of ferritin and apoferritin (**3–5**), the main component of the crystallization driving force stems from the strong Cd^{2+} -mediated bond between each pair of molecules. The unexpected part of our conclusion is that this driving force is not of enthalpy origin (the likely large negative enthalpy of such a bond must have been compensated for by unfavorable enthalpy effects of other patches of the molecules), but comes from the entropy of the water released during the formation of this bond.

6. Molecular-Level Kinetics of Growth

While the kink density is a thermodynamic growth variable that characterizes the affinity of the crystal to the solute molecules, the kinetics of incorporation are reflected by the flux of molecules into a growth site. To monitor these fast incorporation events, we disabled the slow scanning axis of the atomic force microscope. The advance of a step site is shown in **Figs. 8** and **9**. Area scans immediately following the trace in **Figs. 8** and **9** revealed that step motion is not inhibited or accelerated at the location of scanning; that is, the chosen scanning parameters ensured that step propagation was not affected by scanning over the same line for approx 3 min.

Despite the relatively high solution supersaturation $\sigma = 1.1$, the time trace in **Fig. 8** reveals not only 25 arrivals to, but also 22 departures of molecules from the monitored site. All arrivals and departures of molecules to and from the monitored site involve single molecules. Thus, in contrast to claims of pre-formed multiple-molecule growth units for the protein lysozyme (**63–65**), apoferritin and ferritin crystal grow by the attachment of single molecules.

This type of data collection does not allow observations of the neighboring sites at the step. Hence, we cannot distinguish between attachment and detachment from molecules in the kinks or at the steps. Still, we notice that the resi-

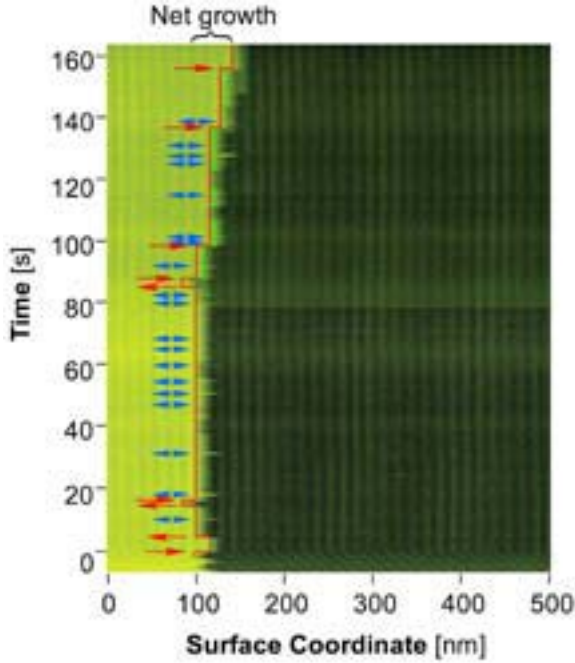


Fig. 8. Incorporation of molecules into steps at apoferritin concentration of 70 mg/mL, $\sigma = 1.1$, and $(C/C_e - 1) = 2.04$. The pseudoimage recorded using a scanning frequency of 3 Hz with the y scan axis disabled at time = 0 shows displacement of one step site. The contour traces the step position. Red arrows indicate attachment and detachment events with a residence time > 1 s, and blue double-sided arrows with a residence time < 1 s; for details, see the text. The appearance of $1/2$ molecule attachments at times > 80 s, highlighted in green, is owing to events at a neighboring site that entered the image owing to scanner drift. (From **ref. 10.**)

dence times t between these events fall into either $t \leq 1$ s or $t > 5$ s. **Figure 8** shows six events of the second type and 19 events of the first. Their ratio is roughly equal to the kink density along the step, suggesting that the longtime events may be attachments and detachments to and from a kink, and the short ones may be sightings of molecules at the step edge.

Furthermore, molecules may enter the line of observation owing to molecular diffusion along the step, or to exchange with the terrace between the steps or the adjacent solution. Whereas the latter results in step propagation and growth, the former is a process that only involves rearrangement of molecules already belonging to the crystals and that may not be associated with growth. To distinguish between the two, as done previously for steps on metal and semiconductor surfaces (28,54,66–68), we calculated the time correlation func-

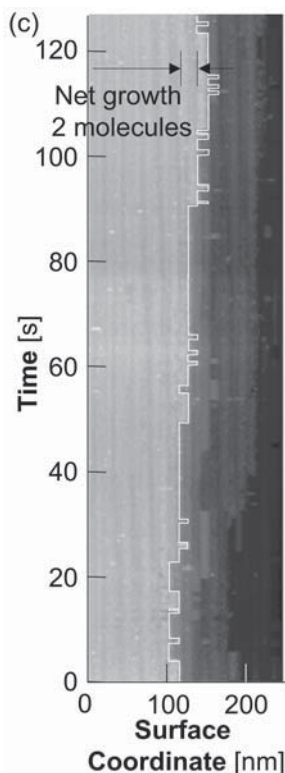


Fig. 9. Incorporation of molecules into steps on ferritin crystal at protein concentration of 70 mg/mL, corresponding to supersaturation $\sigma = \Delta\mu/k_B T = 0.7$, $(C/C_e - 1) = 1$. A pseudocolor image recorded with the scan axis parallel to the step disabled at time = 0 shows the displacement of one molecular site at the step. In this imaging mode, the molecules in the upper and lower layers appear as vertical columns. The red contour traces the step position. Left shifts of this contour indicate detachment of a molecule from the monitored site, and right shifts indicate molecular attachment into the monitored site. (From **ref. 31**.)

tion of the step position x (in molecular size units) as $([x(t + \Delta t) - x(t)]^2)_{\Delta t}$, with averaging over the respective Δt . In **Fig. 10**, it is plotted as a function of Δt . Theoretical analyses of the exchange of the steps with the medium at equilibrium (28,54,68–70) predict that if diffusion along the step edge dominates the advance of the step site, the cross-correlation should follow $\Delta t^{1/4}$ dependence (28,54,68–70). We found no theory dealing with supersaturated conditions. However, motion of a site on the step edge is similar to Brownian motion (68,69). For Brownian diffusion, the coefficient relating $([x(t + \Delta t) - x(t)]^2)_{\Delta t}$ and $\Delta t^{1/2}$ may vary, but the exponent 1/2 of Δt does not depend on the presence

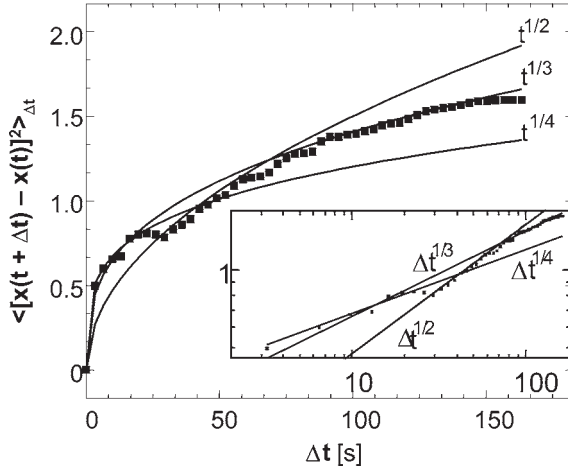


Fig. 10. Time correlation curve, characterizing mean square displacement of a location at a step for a time interval Δt as a function of this Δt , corresponding to trace of step location in **Fig. 8**; inset: logarithmic plot. Solid squares indicate data; lines fits with exponential dependencies on time as indicated in the plots. (From **ref. 25**.)

or absence of concentration/chemical potential gradients (57). Hence, we use only the exponents of Δt stemming from the data in **Fig. 10** for further discussion.

The data in **Fig. 10** do not fit a single exponential. The deviation from $1/4$ at times longer than 20 s allows us to conclude that the trace in **Fig. 8** likely reflects exchange of molecules between the step and interstep terraces or the adjacent solution. This conclusion allows us to extract from **Figs. 8** and **9** net frequencies of attachment of molecules to kinks. For apoferritin at $(C/C_e - 1) = 2$, from the net attachment of three molecules for 162 s and the probability of viewing a kink of $1/n_k = 1/3.5$, we get $(j_+ - j_-) = 0.065 \text{ s}^{-1}$, or one molecule per approx 15 s. For ferritin at $(C/C_e - 1) = 1$, **Fig. 9** shows net growth of two molecules for 128 s, leading to an average net flux $(j_+ - j_-) = 0.054 \text{ s}^{-1}$ into the growth sites distributed with mean density = 0.28. Thus, even at the relatively high supersaturation in **Figs. 8** and **9**, incorporation of molecules into the crystal is extremely slow and occurs over macroscopic time scales

The step velocities v for the two proteins, determined using the three methods discussed in **Subheading 2.3**, are shown in **Fig. 11**. The data fit well the proportionality

$$v = \beta \Omega C_e (C/C_e - 1) = \beta \Omega n_e (n/n_e - 1) \quad (16)$$

with $\Omega = 1/4 a^3 = 1.56 \times 10^{-18} \text{ cm}^3$ —the crystal volume per ferritin or apoferritin molecule, and step kinetic coefficient β (50,71) is $(6.0 \pm 0.4) \times 10^{-4} \text{ cm/s}$ for ferritin and $(6.0 \pm 0.3) \times 10^{-4} \text{ cm/s}$ for apoferritin.

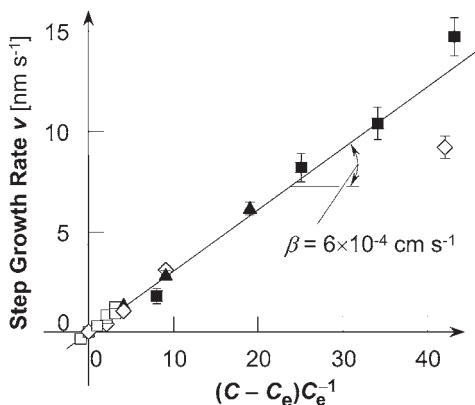


Fig. 11. Determination of kinetic coefficients for step growth for ferritin and apoferritin. Dependencies of the step growth rates v on the crystallization driving force $(C/C_e - 1)$. (\square , \diamond) v -Values for, respectively, ferritin and apoferritin, from sequences of molecular resolution *in situ* AFM images of the advancing steps. The reason for the lower value of the point for apoferritin at $(C/C_e - 1) = 42$ is not well understood. This point was not used in the determination of the kinetic coefficient β . (\blacktriangle) Data for apoferritin extracted from disabled y-axis scans. (\blacksquare) Data for ferritin from time traces of the step growth rate using laser interferometry. The straight line corresponds to the step kinetic coefficient $\beta = 6 \times 10^{-4}$ cm/s. (From ref. 40.)

Since there are no sources or sinks of molecules at the step other than the attachment sites, the step growth rate v should equal $\bar{a}\bar{n}_k^{-1}(j_+ - j_-)$ (50,72). At $(C/C_e - 1) = 1$, at which all data on ferritin in Fig. 9 were collected, the value of the step growth rate for ferritin from Fig. 11 is $v = 0.20$ nm/s, equal to the product $\bar{a}\bar{n}_k^{-1}(j_+ - j_-)$. For apoferritin, the average step velocity at $(C/C_e - 1) = 2$, $\sigma = 1.1$ is $v = 0.26$ nm/s. The product $\bar{a}\bar{n}_k^{-1}(j_+ - j_-)$ determined at the same conditions is 0.24 nm/s.

The closeness of the values of the product $\bar{a}\bar{n}_k^{-1}(j_+ - j_-)$ and measured v s indicates that the step propagation in ferritin crystallization occurs only owing to incorporation of molecules into the kinks along the steps (10,25).

7. What Limits the Rate of Incorporation of a Molecule in a Kink?

7.1. Diffusion-Limited or Transition-State Kinetics

Next, I discuss the factors that determine the rate of the last stage, the chemical stage, in the growth mechanism—the incorporation into a kink of a molecule standing in front of this kink. In this way, I eliminate from consideration the rate of supply of the molecules from the solution bulk to the kink, constituting the transport stage of the growth mechanism.

The kinetics of chemical reactions in solutions are either limited only by the rate of diffusion of the species (73) or additionally slowed down by a high-energy transition state (74). The former kinetics pathway does not exclude the presence of potential free-energy barriers. It has been shown that if molecules have to overcome a repulsive maximum to reach the bonding minimum, the rate of binding can be evaluated as diffusion over the barrier. The resulting kinetic law contains an exponential dependence on the height of the barrier (74).

For the kinetics of the phase transitions in solutions, it is generally accepted that colloid particles follow the diffusion-limited model, while the growth rates of new phases of small molecules are thought to be governed by a transition state (71,72,75–77). For the intermediate case of protein solid phases, the growth kinetics largely resemble those of small molecules, and it was assumed that transition-state laws apply (78). Although rate laws reminiscent of diffusion-limited mechanisms have been postulated for small-molecule phase transitions (49,79,80), they were viewed as equivalent to respective transition-state expressions (79,80), and no critical tests to discriminate between the two mechanisms were suggested or performed.

In the transition-state kinetics, the rate coefficients are (1) mass dependent (50,81); (2) independent on the diffusivity (74); and (3) faster for high-symmetry molecules, because of the transition-state entropy (72). I discuss next evidence indicating that (no. 1) is violated for the ferritin/apoferritin pair of proteins, and that nos. 2 and 3 are violated for many other systems, suggesting that the rate of many phase transitions is in fact diffusion limited.

The data in Fig. 11 show that at equal driving forces, the step growth rates are equal for the two proteins. Since in the preceding subsections we have shown that the mechanism of attachments of molecules to kinks are identical for the two proteins, we conclude that this observation is in apparent contradiction with transition-state-type kinetic laws, in which the vibrational components of the transition-state partition function lead to proportionality of β to $m^{-1/2}$, characteristic of no. 1 of the transition-state kinetics just discussed. We conclude that the kinetics of incorporation into the kinks are only limited by diffusion (40).

7.2. Evaluation of Flux of Molecules Into a Kink in the Case of Diffusion-Limited Kinetics

We derive an expression for the kinetic coefficient of growth of crystals from solution as diffusion over an energy barrier U , followed by unimpeded incorporation (73,74). The barrier U may be of electrostatic origin (74); however, for the ferritin/apoferritin pair, it probably accounts for the need to expel the water molecules attached to the incoming molecules and to the growth site (82). Repulsive potentials owing to water structuring at hydrophobic and hydrophilic surface patches can have significant strength and range (83,84).

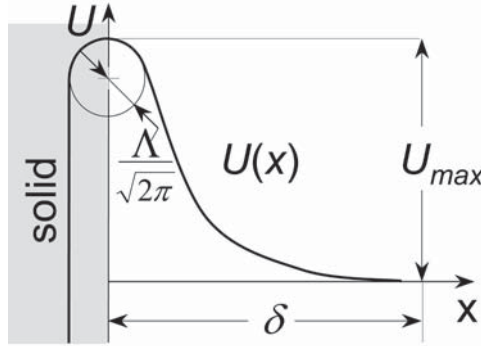


Fig. 12. Schematic illustration of the potential energy relief in front of growth interface. For details, see the text. (From **ref. 40**.)

In **Fig. 12**, the resulting potential relief is schematically depicted. The potential reaches its maximum value U_{\max} at the crossing of the increasing branch, owing to the repulsion between the incoming solute molecules and the crystal surface at medium separations, and the receding branch, which corresponds to the short-range attraction required if the molecules should enter the growth site. We position the beginning of the coordinate axis $x = 0$ at the location of this maximum. We assign a finite curvature of $U(x)$ about this maximum and link it with the expulsion of the last few solvent molecules as an incoming solute molecule joins the crystal. The finite curvature assumption follows previous solutions to similar problems (85,86). The distance d , used as the upper integration limit, is bound from below by the range of interaction of the solute molecules with the surface, which can be a few solute molecular sizes, and from above by the distances between the solute molecules in the solution bulk, $n^{-1/3} \approx 0.2$ nm. Thus, d can be chosen significantly longer than the molecular sizes and kink lengths, and using a one-dimensional model is justified. Since the rate of diffusion over a sharp barrier only depends on the curvature around the maximum (85,86), the choice of d does not affect the result

To calculate the flux J of molecules with concentration n that, driven by a concentration gradient, overcome a barrier to reach the surface, we orient the coordinate x perpendicular to a growing surface and denote the potential relief close to this surface as $U(x)$. From the generalized Fick law, $J = (nD/k_B T) d\mu/dx$, with $\mu(T, x) = \mu_0(T) + k_B T \ln[\gamma n(x)] + U(x)$ and $\gamma \approx 1$ (10), J is linked to $U(x)$, $n(x)$ and the gradient of n as (73,86)

$$J = D \left\{ \frac{dn(x)}{dx} + n(x) \frac{d[U(x)/k_B T]}{dx} \right\}, x > 0 \quad (17)$$

with D being the Stokes diffusion coefficient of the molecules. In search of a steady $J = \text{const}$, we integrate **Eq. 17** with two sets of boundary conditions: (1) that at a certain distance from the surface δ , $x \geq \delta$, $U = 0$, and $n = n_\delta$; and (2) that in the crystal, i.e., at $x \leq 0$, $n = 0$.

Dividing by D and multiplying both sides by $\exp[U(x)/k_B T]$, we get

$$\frac{J}{D} \exp[U(x)/k_B T] = \frac{d}{dx} \left\{ n(x) \exp[U(x)/k_B T] \right\} \quad (18)$$

Integrating from $x = 0$ to $x = \delta$, using the boundary conditions at $x = 0$ and $x \geq \delta$, we get

$$J = \frac{n_\delta D}{\int_0^\delta \exp[U(x)/k_B T] dx} \quad (19)$$

an analog to equation 9.51 in **ref. 74** and the Fuchs expression for coagulation of particles interacting through $U(x)$.

If $U(x)$ has a sharp maximum at $x = 0$, we can represent it with a symmetric function around the point of the maximum. As shown below, in many cases $|d^2 U/dx^2| < a$, and this justifies the assumption of a sharp maximum. We use only the first two members of the Taylor series: $U(x) = U_{\text{max}} - 1/2 d^2 U/dx^2 |x|^2$. The minus sign stems from $d^2 U/dx^2 < 0$ at the maximum. Then, the integral

$$\int_0^\delta \exp[U(x)/k_B T] dx \cong \exp\left(\frac{U_{\text{max}}}{k_B T}\right) \left[\frac{2}{\pi} \left| \frac{\partial^2 (U/k_B T)}{\partial x^2} \right|_{x=0} \right]^{-1/2} \quad (20)$$

The approximate equality above is based on $\delta \gg [1/2 d^2 U/dx^2]^{-1/2}$, the half-width of the Gaussian function in **Eq. 20**. Finally,

$$J = D \sqrt{\frac{2}{\pi k_B T}} \left\{ \left| \frac{\partial^2 U}{\partial x^2} \right|_{\text{max}} \right\}^{1/2} \exp\left(-\frac{U_{\text{max}}}{k_B T}\right) n_\delta \quad (21)$$

Note that only half of the flux J from **Eq. 21** contributes to growth: on top of the barrier, the force driving the molecules into the crystal is zero, and a molecule has equal chances of getting incorporated, or going back to the solution (87). With this, and introducing the parameter L as the radius of curvature of $U(x)/k_B T$ at its maximum

$$\Lambda = \left(\frac{1}{2\pi} \left| \frac{\partial^2 (U/k_B T)}{\partial x^2} \right|_{\text{max}} \right)^{-1/2} \quad (22)$$

the expression for J becomes

$$J = \frac{D}{\Lambda} \exp\left(-\frac{U_{\max}}{k_B T}\right) n_\delta \quad (23)$$

Equation 23 is essentially identical to the nucleation rate expression derived by Zeldovich (86) as a diffusion flux over a potential barrier in the space of cluster sizes.

If U_{\max} is owing to the hydration of the incoming molecule and the site where it attaches, the radius of curvature of $U(x)$ around U_{\max} should be the size of a few water molecules, 2 to 4 Å, and the length Λ should be approx 5–10 Å. Note that in this evaluation, we apply discrete considerations to a continuous model. Still, we expect the estimate of Λ to be roughly correct.

If all molecules that overcome the barrier are incorporated into a kink, the incoming flux into a kink is $j_+ = JDS_{\text{kink}} \approx Ja^2$, in which a^2 is an effective surface area of a kink. If there are no solute transport constraints (kinetic growth regime), n_d is equal to that in the solution bulk n . Furthermore, in equilibrium, when n equals the solubility, n_e , $j_+ = j_-$. Since j_- does not depend on n in the solution, the step velocity v is

$$v = \frac{a}{n_k} (j_+ - j_-) = \frac{a^3}{n_k} \frac{D}{\Lambda} \exp\left(-\frac{U_{\max}}{k_B T}\right) (n - n_e) \quad (24)$$

Because Brownian diffusion does not depend on the molecular mass, the above model yields a mass-independent kinetic coefficient (for details, see the supplementary information). The resulting step growth rate v is

$$v = \frac{a}{n_k} (j_+ - j_-) = \frac{a^3}{n_k} \frac{D}{\Lambda} \exp\left(-\frac{U_{\max}}{k_B T}\right) (n - n_e) \quad (25)$$

in which L contains the radius of curvature of $U(x)$ around its maximum and, hence, is likely the size of a few water molecules, approx 5–10 Å.

With $a^3 = W$, we can rewrite **Eq. 25** in the typical form of **Eq. 16** that is readily comparable to experimental data (40). This defines β as

$$\beta = \frac{1}{n_k} \frac{D}{\Lambda} \exp\left(-\frac{U_{\max}}{k_B T}\right) \quad (26)$$

The parameters in this expression, \bar{n}_k , D , Λ , and U_{\max} , have a clear physical meaning and can be independently measured (40).

7.3. How Broad Is the Class of Molecules That Follow Diffusion-Limited Kinetics Law?

The ratio $D/\Lambda\bar{n}_k$ has been used (88) as a kinetic coefficient for crystallization from the melt, with L defined as the “free path” of the building blocks, atoms, or molecules in the melt. In further work, this law was shown to poorly predict the behavior of metals during solidification (89). Note that in contrast to the above expression for melt growth, **Eq. 26** treats growth from solutions with Einstein-Stokes diffusion of the solute molecules.

In a classic paper (49), the ratio of the diffusivity to the mean distance between kinks, $D/\Lambda\bar{n}_k$, was used as a kinetic coefficient. This definition misses the energy barrier for growth, demonstrated by numerous later experiments (81). In a further development (79), the kinetic coefficients for motion of steps were postulated as $\beta = (D/\Lambda)\exp(-U/k_B T)$, with Λ introduced as a “jump length in the solution.” Comparing this formula with our **Eq. 26**, we see that **Eq. 26** explicitly accounts for the mean kink density \bar{n}_k^{-1} and provides a clear definition of Λ .

Evidence for diffusion-limited kinetics in other solution crystallization systems can be found in experiments on growth of protein crystals in gels, in which the protein diffusivity is significantly lower than in a “free” solution. It was found with two proteins that the maximum value of the growth rate, recorded at the early stages of growth before solution depletion and transport control set in, is 1.5 to 3 times lower than the equivalent value in free solutions (90). This suggests that the kinetic coefficient of growth is correlated to the diffusivity. In another work with the protein lysozyme, it was found that in gelled media, the protein concentration at the growth interface is essentially equal to the one in free solutions, while the concentration gradient at the interface, proportional to the growth rate, is lower by approx 1.5 times (91). This is only possible if the kinetic coefficient in gels is lower, supporting the correlation between β and D and contradicting characteristic no. 2 of the transition-state kinetic laws, discussed in **Subheading 7.1**.

Table 1 shows that the known kinetic coefficients for crystallization of about a dozen proteins, protein complexes, and viri are in the range of 0.8 to 400×10^{-4} cm/s (17,22,25,92,93). The molecular symmetry groups have orders ranging from 1 to 3, to 24 for the ferritins, and 60 for the satellite tobacco mosaic virus. No correlation exists between higher molecular symmetry and higher kinetic coefficients. This suggests that the rate-limiting step is not the decay of a transition state that should be facilitated for high-symmetry molecules with higher transition-state entropies, characteristic no. 3 discussed in **Subheading 7.1**.

Evidence in favor of the applicability of the diffusion-limited kinetics also applies for phase transitions involving small-molecule substances and comes from detailed data on the adsorption kinetics on the surface of a growing

Table 1
Kinetic Coefficients (β), Diffusivities (D),
Effective Molecular Diameter (a), Point Symmetry Group of Molecule (G),
and Order of Symmetry Group (Z) for Various Systems

System	β , 10^{-4} (cm/s)	D , 10^{-6} (cm ² /s)	a (nm)	G	Z	Reference
Insulin			6.5	$\bar{3}m$	6	103
No acetone	90	0.79				
approx 5% acetone	420					
Apo ferritin	6	0.32	13	432	24	25
Ferritin	6	0.32	13	432	24	40
Canavalin, R3 form	5.8–26	0.4	3.5–8	3	3	22
Lumasine synthase	3.6	0.16	18	m5	60	O. Gliko, unpublished
Catalase	0.32	NA ^a	11.5	222	4	104
Lysozyme (101)		0.73	3	1	1	
Typical	2–3					105
No step bunching	22–45					93
Lysozyme (110)	2–3					106
STMV	4–8	0.2	16	m5	60	17
Thaumatococcus	2	0.6	4.0	1	1	107
Various inorganic systems (ADP, KDP, alums, etc.)	~100–1000	~1–5	0.5	1, 2, $\bar{2}$, m, etc.	1, 2	108

^aNA, not available; ADP, ammonium-dihydrogen phosphate; KDP, potassium-dihydrogen phosphate.

ammonium-dihydrogen phosphate (ADP) crystal (**94,95**). The data for the temperature range of 29–67°C were fitted to an equivalent of **Eq. 26** with $\bar{n}_k^{-1} = 1$ to account for the suspected density of the adsorption sites (**94,95**); for the surface diffusion mechanism selected by this system, adsorption is the process to be limited by either diffusion or a transition-state decay rate. The fit yielded $\Lambda = 13 \text{ \AA}$ and $U = 27 \text{ kJ/mol}$. The closeness of L to the range just suggested for the diffusion-limited case suggests that this mechanism is the rate-determining one for the investigated phase transition.

Further evidence in favor of the applicability of this mechanism to small molecules comes from the unusually narrow grouping of the kinetic barriers for growth of approx 10 diverse substances at $28 \pm 7 \text{ kJ/mol}$ (**81**). The chemical nature of these substances ranges from inorganic salts, to organic molecular compounds, to proteins and viri. Hence, the narrow range of the activation barriers is unexpected for transition-state kinetics, in which the activated com-

plexes should reflect the chemical variety of the crystallizing compounds. On the other hand, assuming diffusion-limited kinetics, we note that the diffusivities in aqueous solutions have effective activation energies of approx 8–17 kJ/mol (38,96). If, as suggested by Eq. 26, we subtract these values from the barriers of 28 ± 7 kJ/mol (81), characterizing the overall kinetics, only approx 10–20 kJ/mol remain for the barriers owing to the interactions between the solute and the crystal surface. The range of 28 ± 7 kJ/mol is sufficiently broad to accommodate the chemical specificity of the solutes.

Thus, our experimental data in the context of other recent findings show that the kinetics of attachment of molecules to a growing phase during crystallization or other phase transitions in solution are, in many cases, diffusion limited. This applies to proteins, as well as to small-molecule systems. It is important to once again state that this result concerns the kinetics of incorporation of the solute molecules into existing attachments sites. In cases in which such sites are few, or transport from the solution bulk is slow, the kinetics of creation of attachment sites or of transport may control the overall kinetics. What we argue is that after an attachment site exists, and the solute molecules are standing in front of it, the rate of incorporation is solely limited by diffusion, and not restricted by the decay of an intermediate state (40).

8. Molecular Pathway From Solution to Crystal

During crystal growth from solution, the solute molecules have two possible pathways between the solution and the kinks: they can be directly incorporated (49,71), or they can first adsorb on the terraces between the steps, diffuse along them, and then reach the steps (48,49).

If a crystal grows by the direct incorporation mechanism, the competition for supply between adjacent steps is mild (71). By contrast, competition for supply confined to the adsorption phase is acute (79); it retards step propagation and acts as a strong, effective attraction between the steps. This dramatically affects the stability of the step train; the appearance and evolution of step bunches (51); and, ultimately, the crystal's quality and utility (97).

The two mechanisms can be directly discerned by monitoring the adsorbed solute molecules on the crystal surface, similar to experiments with metal atoms at lowered temperatures (98). However, during solution growth at room temperature, the diffusivity of the adsorbed species is approx 10^{-8} cm²/s (22,94); that is, a molecule passes 100 nm in approx 0.01 s. With *in situ* AFM, this distance is covered by the scanning tip typically approx 0.1 s; that is, imaging is too slow to detect and monitor the adsorbed molecules. Electron microscopy of flash-frozen samples has, in several cases, revealed the presence of adsorbed solute molecules on the crystal's surface (99); however, their participation in growth cannot be confidently judged by this technique. Because direct tests

appear impossible, indirect evidence for the growth mechanism of several systems has been sought.

For several solution-grown crystals, the growth mechanism has been deduced by comparing the velocities of isolated steps with those of closely spaced steps. Similar values of the two velocities for silver (100) and calcite (15,16) were taken as evidence for the direct incorporation mechanism. Conversely, slower growth of dense step segments was interpreted in favor of the surface diffusion mechanism for KDP/ADP (21,94), lysozyme (101), and canavalin (22). A known problem for such mesoscale data is that the data sets interpreted in favor of direct incorporation could also reflect a surface diffusion range shorter than the shortest step separation probed (15,16). Thus, critical evidence about the growth mode should be sought by studying the growth processes at the molecular level (10,25).

As shown in **Subheading 7.3.**, in the case of direct incorporation from the solution (*see also refs. 72 and 78*),

$$j_+ - j_- = v_+ C_e \Omega \exp \left(-\frac{U_{\max}}{k_B T} \right) \left[\frac{C}{C_e} - 1 \right], \quad v_+ = \frac{D}{\Lambda a}, \quad \text{and} \quad \frac{j_+}{j_-} = \frac{C}{C_e} \quad (27)$$

Here, U_{\max} is the energy barrier for incorporation into the kinks (50,71); in the case of ferritin, it likely accounts for the need to expel the water molecules structured around hydrophilic patches on the surfaces of the incoming molecules and the molecules forming the kink (82). $\Omega = 1.56 \times 10^{-18} \text{ cm}^3$ is the crystal volume per ferritin molecule; $D = 3.2 \times 10^{-7} \text{ cm}^2/\text{s}$ is the ferritin diffusivity (37); and Λ is the radius of curvature of the surface-molecule interaction potential around its maximum at U_{\max} (73,74) and, hence, should be of the order of a few water molecule sizes, approx 5–10 Å (95). The step velocity v for this growth mode is

$$v = \frac{a}{n_k} (j_+ - j_-) = \frac{\Omega C_e}{n_k} \frac{D}{\Lambda} \exp \left(-\frac{U_{\max}}{k_B T} \right) \left[\frac{C}{C_e} - 1 \right] \quad (28)$$

Analogous considerations for the case of growth via surface diffusion yield for the net flux into the step from the surface are

$$j_{s+} - j_{s-} = v_{s+} n_e a^2 \exp \left(-\frac{U_{s0}}{k_B T} \right) \left[\frac{n_s}{n_e} - 1 \right], \quad v_{s+} = \frac{D_s}{\Lambda_s a}, \quad \text{and} \quad \frac{j_{s+}}{j_{s-}} = \frac{n_s}{n_e} \quad (29)$$

in which n_s and n_e are the surface concentration of adsorbed ferritin and its equilibrium value, respectively; U_{s0} is the energy barrier for incorporation into the kink from the surface; and D_s and Λ_s are, respectively, the surface diffusivity

and curvature of the surface U_s . For the step velocity, one gets through $v = a/\bar{n}_k(j_{s+} - j_{s-})$ an expression analogous to **Eq. 25**.

To evaluate the ratios of the fluxes in and out of step, we use that **Fig. 9** reveals that for ferritin at $C/C_e = 2$, $j_+/j_- \leq 1.105$. For apoferritin, similar experiments in **Fig. 8** show that at $C/C_e = 3$, $j_+/j_- \leq 25/22 = 1.14$. For both proteins, these ratios represent gross violations of the last equality of **Eq. 27**. These violations cannot be attributed to depletion of the solution layer adjacent to the crystal. This factor becomes significant at approx 100 times higher growth rates (**102**) and suggests that the direct incorporation mechanism may not apply. In the case of Langmuir adsorption, $n_s = n_s C(B + C)^{-1}$ (B – Langmuir constant) and $n_s/n_e < C/C_e$. Hence, the lower ratios of the in- to out-flux are compatible with a mechanism of incorporation from the state of adsorption on the surface.

For further tests of the growth mode, we examine the step velocity law in **Eq. 28**. The only unknown parameter here is the energy barrier U_0 . Determinations of v at four temperatures and two ferritin concentrations in **Fig. 13** yield $E_{\text{total}} = 41 \pm 3$ kJ/mol. In **Eq. 28**, C_e (**56**) and Ω do not depend on temperature, and Λ is about the size of a few water molecules and in a first approximation does not depend on T (**95**). For a molecule following the Stokes law, $D = D_0 \exp(-E_{\text{visc}}/k_B T)$, where E_{visc} is the temperature factor in an Arrhenius-type expression for the dependence of the solvent viscosity on temperature. For NaCl solutions in Na acetate buffer, $E_{\text{visc}} = 7.4$ kJ/mol (**38**). As shown in **Eq. 28**, \bar{n}_k has a weak near-exponential dependence on T through the kink energy $w = 3.8$ kJ/mol. This leaves $U_0 \approx 30$ kJ/mol. This value is close to the 28 kJ/mol found as the average over systems ranging from inorganic salts, through organics, to proteins and viri (**81**).

Substituting into **Eq. 28**, we get at $C/C_e = 2$, $v = 0.0014$ nm/s, and at $C/C_e = 3$, $v = 0.0028$ nm/s. These values are more than two orders of magnitude lower than actually observed. The measured values of 0.20 and 0.31 nm/s would require $U_{\text{max}} \approx 18$ kJ/mol, beyond the range of the determination in **Fig. 13**. This discrepancy supports the assertion that the direct incorporation mechanism is inapplicable to the growth of ferritin. We conclude that a mechanism involving adsorption on the terraces better corresponds to the available data for ferritin. As noted, in the ferritin/apoferritin system, the steps only exhibit attraction at very short separations. We conclude that the characteristic surface diffusion length (**49**) must be shorter than a few lattice parameters to account for this. Note that an investigation limited to data on the mesoscale step kinetics would have concluded that the growth mechanism is direct incorporation.

A relevant question is: why do the energetics of the system select the surface diffusion mechanism over the direct incorporation? This question can only be addressed with the molecular-level data available for the system. We note that when the surface diffusion mechanism operates, the energy barrier determined

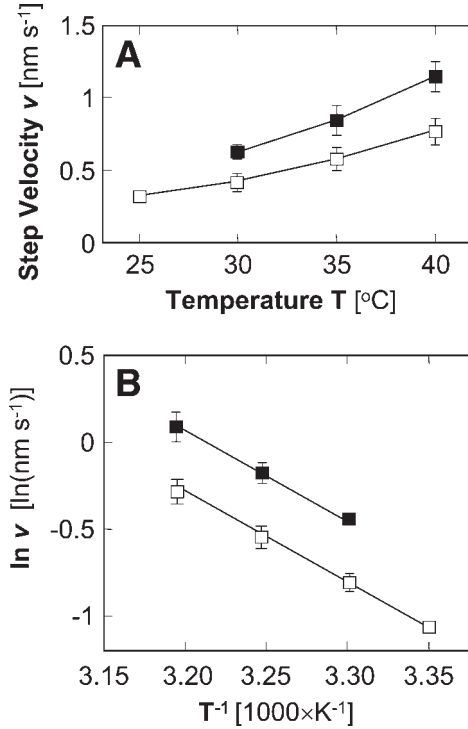


Fig. 13. Dependencies of step velocity v for growth of ferritin on temperature (A), and in Arrhenius coordinates (B). (■) at $C/C_e = 4$; (□) at $C/C_e = 3$. For each point, positions of advancing steps were compared in sequences of molecular resolution *in situ* AFM images; approx 20 such determinations of v were averaged. The error bars represent the 90% confidence interval of the average. (From ref. 31.)

from the data in **Fig. 13** is a function of the barriers of the elementary steps of this mechanism and should be denoted as U_{sum} . As shown in **refs. 79 and 95**, $U_{\text{sum}} = U_{\text{ads}} - U_{\text{desorb}} + U_{\text{SD}} + U_{\text{step}}$, which are the barriers, respectively, for adsorption, desorption, surface diffusion, and incorporation into the step (*see Fig. 14*). Since the energy effect of one intermolecular bond of ferritin should be equal to that of apoferritin, $\phi \approx 3k_B T = 7.4$ kJ/mol (25), we can safely assume that for adsorption – desorption on a (111) f.c.c. surface, $U_{\text{ads}} - U_{\text{desorb}} = DH_{\text{ads}} = -3\phi = -22$ kJ/mol. When interactions between the adsorbed molecules are ignored, the lowest possible value of U_{SD} occurs when only one bond is broken on passage between two adsorption sites; hence, $U_{\text{SD}} \geq \phi$. This yields $U_{\text{step}} \leq 44$ kJ/mol, similar to the ADP value (95). Since an equal number of bonds, three, are created during adsorption and incorporation into the step, we can roughly assume $U_{\text{ads}} \approx U_{\text{step}}$. Thus, the highest barrier encountered by a

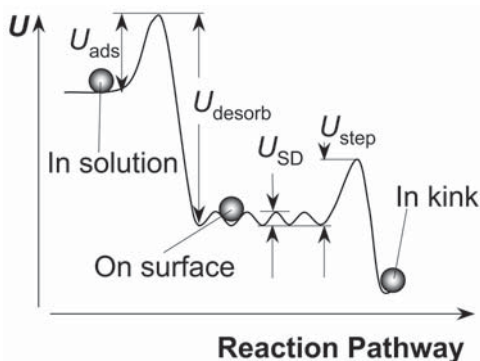


Fig. 14. Energy landscape of surface diffusion mechanism. For notations, see the text. (Modified from **ref. 109.**)

molecule en route to the kink is ≤ 44 kJ/mol. For direct incorporation into kinks, for which all of the six bonds are created simultaneously, $U_{\text{kink}} \sim U_{\text{ads}} + U_{\text{step}} \approx 88$ kJ/mol. A crude estimate yields that this would make growth via this pathway slower by a factor of $\sim \exp[(88,000 - 44,000)/RT] \sim 10^8$.

Acknowledgments

These studies would not have been possible without the dedicated work of my collaborators who took part in the original investigations reviewed here: S. T. Yau, K. Chen, and D. Petsev. I thank O. Galkin for critical comments on the manuscript. Generous financial support throughout the years has been provided by the Office of Biological and Physical Research, NASA.

References

- 1 Theil, E. C. (1987) Ferritin: structure, gene regulation, and cellular function in animals, plants and microorganisms. *Annu. Rev. Biochem.* **56**, 289–315.
- 2 Massover, W. H. (1993) Ultrastructure of ferritin and apoferritin: a review. *Micron* **24**, 389–437.
- 3 Harrison, P. M. and Arosio, P. (1996) The ferritins: molecular properties, iron storage function and cellular regulation. *Biochim. Biophys. Acta* **1275**, 161–203.
- 4 Lawson, D. M., Artymiuk, P. J., Yewdall, S. J., et al. (1991) Solving the structure of human H ferritin by genetically engineering intermolecular crystal contacts. *Nature* **349**, 541–544.
- 5 Hempstead, P. D., Yewdall, S. J., Fernie, A. R., Lawson, D. M., Artymiuk, P. J., Rice, D. W., Ford, G. C., and Harrison, P. M. (1997) Comparison of the three dimensional structures of recombinant human H and horse L ferritins at high resolution. *J. Mol. Biol.* **268**, 424–448.
- 6 Taft, K. L., Papaefthymiou, G. C., and Lippard, S. J. (1993) A mixed-valent polyiron oxo complex that models the biomineralization of the ferritin core. *Science* **259**, 1302–1305.

- 7 Pereira, A. S., Tavares, P., Lloyd, S. G., Danger, D., Edmondson, D. E., Theil, E. C., and Huynh, B. H. (1997) Rapid and parallel formation of Fe³⁺ multimers, including a trimer, during H-type subunit ferritin mineralization. *Biochemistry* **36**, 7917–7927.
- 8 Gider, S., Awschalom, D. D., Douglas, T., Mann, S., and Chaparala, M. (1995) Classical and quantum magnetic phenomena in natural and artificial ferritin proteins [see comments]. *Science* **268**, 77–80.
- 9 Yang, D. and Nagayama, K. (1995) Permeation of small molecules into the cavity of ferritin as revealed by proton nuclear magnetic resonance relaxation. *Biochem. J.* **307**, 253–256.
- 10 Yau, S. T., Petsev, D. N., Thomas, B. R., and Vekilov, P. G. (2000) Molecular-level thermodynamic and kinetic parameters for the self-assembly of apoferritin molecules into crystals. *J. Mol. Biol.* **303**, 667–678.
- 11 Hansma, P. K., Cleveland, J. P., Radmacher, M., et al. (1994) Tapping mode atomic force microscopy in liquids. *Appl. Phys. Lett.* **64**, 1738–1740.
- 12 Noy, A., Sanders, C. H., Vezenov, D. V., Wong, S. S., and Lieber, C. M. (1998) Chemically sensitive imaging in tapping mode by chemical force microscopy: relationship between phase lag and adhesion. *Langmuir* **14**, 1508–1511.
- 13 Durbin, S. D. and Carlson, W. E. (1992) Lysozyme crystal growth studied by atomic force microscopy. *J. Crystal Growth* **122**, 71–79.
- 14 Durbin, S. D., Carson, W. E., and Saros, M. T. (1993) In situ studies of protein crystal growth by atomic force microscopy. *J. Phys. D: Appl. Phys.* **26**, B128–B132.
- 15 Hillier, P. E., Manne, S., Hansma, P. K., and Gratz, A. J. (1993) Atomic force microscope: a new tool for imaging crystal growth processes. *Faraday Discuss.* **95**, 191–197.
- 16 Gratz, A. J., Hillner, P. E., and Hansma, P. K. (1993) Step dynamics and spiral growth on calcite. *Geochim. Cosmochim. Acta* **57**, 491–495.
- 17 Malkin, A. J., Land, T. A., Kuznetsov, Y. G., McPherson, A., and DeYoreo, J. J. (1995) Investigation of virus crystal growth mechanism by in situ atomic force microscopy. *Phys. Rev. Lett.* **75**, 2778–2781.
- 18 McPherson, A., Malkin, A. J., and Kuznetsov, Y. G. (1995) The science of macromolecular crystallization. *Structure* **3**, 759–768.
- 19 Malkin, A. J., Kuznetsov, Y. G., Land, T. A., DeYoreo, J. J., and McPherson, A. (1996) Mechanisms of growth of protein and virus crystals. *Nat. Struct. Biol.* **2**, 956–959.
- 20 Ng, J. D., Kuznetsov, Y. G., Malkin, A. J., Keith, G., Giege, R., and McPherson, A. (1997) Visualization of RNA crystal growth by atomic force microscopy. *Nucleic Acids Res.* **25**, 2582–2588.
- 21 De Yoreo, J. J., Land, T. A., and Dair, B. (1994) Growth morphology of vicinal hillocks on the {101} face of KH₂PO₄: from step flow to layer-by-layer growth. *Phys. Rev. Lett.* **73**, 838–841.
- 22 Land, T. A., DeYoreo, J. J., and Lee, J. D. (1997) An in-situ AFM investigation of canavalin crystallization kinetics. *Surf. Sci.* **384**, 136–155.

- 23 Yip, C. M. and Ward, M. D. (1996) Atomic force microscopy of insulin single crystals: direct visualization of molecules and crystal growth. *Biophys. J.* **71**, 1071–1078.
- 24 Yip, C. M., DePhelippis, M. R., Frank, B. H., Brader, M. L., and Ward, M. D. (1998) Structural and morphological characterization of ultralente insulin crystals by atomic force microscopy: evidence of hydrophobically driven assembly. *Biophys. J.* **75**, 1172–1179.
- 25 Yau, S. T., Thomas, B. R., and Vekilov, P. G. (2000) Molecular mechanisms of crystallization and defect formation. *Phys. Rev. Lett.* **85**, 353–356.
- 26 Lin, H., Yau, S. T., and Vekilov, P. G. (2003) Dissipating step bunches during crystallization under transport control. *Phys. Rev. E* **67**, 0031606.
- 27 Giesen-Seibert, M., Jentjens, R., Poensgen, M., and Ibach, H. (1993) Time dependence of step fluctuations on vicinal copper (111) surfaces investigated by tunneling microscopy. *Phys. Rev. Lett.* **71**, 3521–3524.
28. Poensgen, M., Wolf, J., Frohn, J., Giesen, M., and Ibach, H. (1992) Step dynamics on Ag(111) and Cu(100) surfaces. *Surf. Science* **274**, 430–440.
29. Kitamura, N., Lagally, M. G., and Webb, M. B. (1993) Real-time observations of vacancy diffusion on Si(001)-(2x2) by scanning tunneling microscopy. *Phys. Rev. Lett.* **71**, 2081–2085.
- 30 Swartzentruber, B. S., Mo, Y. W., Kariotis, R., Lagally, M. G., and Webb, M. B. (1990) Direct determination of site and kink energies of vicinal Si(001). *Phys. Rev. Lett.* **65**, 1913–1916.
- 31 Chen, K. and Vekilov, P. G. (2002) Evidence for the surface diffusion mechanism of solution crystallization from molecular-level observations with ferritin. *Phys. Rev. E* **66**, 021606.
32. Choi, S. C. (1978) *Introductory Applied Statistics in Science*, Prentice Hall, Englewood Cliffs, NJ.
- 33 Vekilov, P. G., Alexander, J. I. D., and Rosenberger, F. (1996) Nonlinear response of layer growth dynamics in the mixed kinetics-bulk transport regime. *Phys. Rev. E* **54**, 6650–6660.
- 34 Gliko, O., Booth, N. A., Rosenbach, E., and Vekilov, P. G. (2002) Phase-shifting interferometry for the study of the step dynamics during crystallization of proteins. *Crystal Growth Design* **2**, 381–385.
- 35 Gliko, O., Booth, N. A., and Vekilov, P. G. (2002) Step bunching in a diffusion-controlled system: phase-shifting interferometry investigation of ferritin. *Acta Crystallogr. Sect. D* **58**, 1622–1627.
36. Gliko, O. and Vekilov, P. G. (2002) Spatio-temporal step patterns during crystal growth in a transport controlled system. *J. Phys. Chem.* **106**, 11,800–11,804.
- 37 Petsev, D. N., Thomas, B. R., Yau, S. T., and Vekilov, P. G. (2000) Interactions and aggregation of apoferritin molecules in solution: effects of added electrolytes. *Biophys. J.* **78**, 2060–2069.
- 38 Fredericks, W. J., Hammonds, M. C., Howard, S. B., and Rosenberger, F. (1994) Density, thermal expansivity, viscosity and refractive index of lysozyme solutions at crystal growth concentrations. *J. Crystal Growth* **141**, 183–192.

- 39 Muschol, M. and Rosenberger, F. (1995) Interaction in undersaturated and supersaturated lysozyme solutions: static and dynamic light scattering results. *J. Chem. Phys.* **103**, 10,424–10,432.
- 40 Petsev, D. N., Chen, K., Gliko, O., and Vekilov, P. G. (2003) Diffusion-limited kinetics of the solution-solid phase transition of molecular substances. *Proc. Natl. Acad. Sci. USA* **100**, 792–796.
41. Sun, S. F. (1994) *Physical Chemistry of Macromolecules*, John Wiley & Sons, New York.
42. Stranski, I. N. (1928) Zur Theorie des Kristallwachstums. *Z. Phys. Chem.* **136**, 259–278.
43. Stranski, I. N. and Kaischew, R. (1934) Über den Mechanismus des Gleichgewichtes kleiner Kriställchen. I. *Z. Phys. Chem.* **B26**, 100–113.
- 44 Kaischew, R. and Stranski, I. N. (1937) Über die Thomson-Gibbs'sche Gleichung bei Kristallen. *Z. Phys. Chem.* **B35**, 427–432.
45. Eisenberg, D. and Crothers, D. (1979) *Physical Chemistry with Applications to Life Sciences*, Benjamin/Cummins, Menlo Park, NJ.
46. Berry, P. S., Rice, S. A., and Ross, J. (2000) *Physical Chemistry*, Oxford University Press, New York.
47. Hill, T. L. (1986) *Introduction to Statistical Thermodynamics*, New York.
48. Volmer, M. (1939) *Kinetik der Phasenbildung*, Steinkopff, Dresden, Germany.
- 49 Burton, W. K., Cabrera, N., and Frank, F. C. (1951) The growth of crystals and equilibrium structure of their surfaces. *Philos. Trans. R. Soc. Lond. Ser. A* **243**, 299–360.
50. Chernov, A. A. (1984) *Modern Crystallography III, Crystal Growth*, Springer, Berlin.
51. Williams, E. D. and Bartelt, N. C. (1991) Thermodynamics of surface morphology. *Science* **251**, 393–400.
52. Chernov, A. A., Rashkovich, L. N., Yamlinski, I. V., and Gvozdev, N. V. (1999) Kink kinetics, exchange fluxes, 1D “nucleation” and adsorption on the (010) face of orthorhombic lysozyme crystals. *J. Phys.:Condens. Matter* **11**, 9969–9984.
- 53 Teng, H. H., Dove, P. M., Orme, C. A., and De Yoreo, J. J. (1998) Thermodynamics of calcite growth: baseline for understanding biomineral formation. *Science* **282**, 724–727.
- 54 Kuipers, L., Hoogeman, M., and Frenken, J. (1993) Step dynamics on Au(110) studied with a high-temperature, high-speed scanning tunneling microscope. *Phys. Rev. Lett.* **71**, 3517–3520.
- 55 Swartzentruber, B. S. (1998) Fundamentals of surface step and island formation mechanisms. *J. Crystal Growth* **188**, 1–10.
- 56 Petsev, D. N., Thomas, B. R., Yau, S.-T., Tsekova, D., Naney, C., Wilson, W. W., and Vekilov, P. G. (2001) Temperature-independent solubility and interactions between apoferritin monomers and dimers in solution. *J. Crystal Growth* **232**, 21–29.
57. Atkins, P. (1998) *Physical Chemistry*, Freeman, New York.

58. Israelachvili, J. N. (1995) *Intermolecular and Surface Forces*, Academic, New York.
59. Eaton, W. A., Munoz, V., Thompson, P. A., Chan, C. K., and Hofrichter, J. (1997) Submillisecond kinetics of protein folding. *Curr. Opin. Struct. Biol.* **7**, 10–14.
60. Tanford, C. (1980) *The Hydrophobic Effect: Formation of Micelles and Biological Membranes*, John Wiley & Sons, New York.
61. Eisenberg, D. and Kauzmann, W. (1969) *The Structure and Properties of Water*, Oxford, New York, University Press.
62. Dunitz, J. D. (1994) The entropic cost of bound water in crystals and biomolecules. *Nature* **264**, 670.
63. Li, M., Nadarajah, A., and Pusey, M. L. (1999) Growth of (101) faces of tetragonal lysozyme crystals: determination of the growth mechanism. *Acta Cryst. Sect. D* **55**, 1012–1022.
64. Li, M., Nadarajah, A., and Pusey, M. L. (1999) Determining the molecular-growth mechanisms of protein crystal faces by atomic force microscopy. *Acta Cryst. Sect. D* **55**, 1036–1045.
65. Nadarajah, A. and Pusey, M. L. (1997) Growth mechanism of the (110) face of tetragonal lysozyme crystals. *Acta Cryst. Sect. D* **53**, 524–534.
66. Alfonso, C., Bermond, J. M., Heyraud, J. C., and Metois, J. J. (1992) The meandering of steps and the terrace width distribution on clean Si(111). *Surf. Sci.* **262**, 371–381.
67. Bartelt, N. C., Einstein, T. L., and Williams, E. D. (1990) The influence of step-step interactions on step wandering. *Surf. Sci. Lett.* **240**, L591–L598.
68. Ihle, T., Misbah, C., and Pierre-Louis, O. (1998) Equilibrium step dynamics of vicinal surfaces revisited. *Phys. Rev. B* **58**, 2289–2309.
69. Pimpinelli, A., Villain, J., Wolf, D. E., Metois, J. J., Heyraud, J. C., Elkinari, I., and Uimin, G. (1993) Equilibrium step dynamics on vicinal surfaces. *Surf. Sci.* **295**, 143–153.
70. Kuipers, L., Hoogeman, M. S., and Frenken, J. W. M. (1995) Step and kink dynamics on Au(110) and Pb(111) studied with a high-speed STM. *Phys. Rev. B* **52**, 11,387–11,397.
71. Chernov, A. A. (1961) The spiral growth of crystals. *Sov. Phys. Uspekhi* **4**, 116–148.
72. Chernov, A. A. and Komatsu, H. (1995) Topics in crystal growth kinetics, in *Science and Technology of Crystal Growth* (van der Eerden, J. P. and Bruinsma, O. S. L., eds.), Kluwer Academic, Dordrecht, The Netherlands, pp. 67–80.
73. Smoluchowski, M. (1916) Drei Vorträge über Diffusion, Brownsche Bewegung und Koagulation von Kolloidteilchen. *Physik Z.* **17**, 557–585.
74. Eyring, H., Lin, S. H., and Lin, S. M. (1980) *Basic Chemical Kinetics*, John Wiley & Sons, New York.
75. Neilsen, A. E. (1967) Nucleation in aqueous solutions, in *Crystal Growth* (Peiser, S., ed.), Pergamon, Oxford, UK, pp. 419–426.

76. Kahlweit, M. (1969) Nucleation in liquid solutions, in *Physical Chemistry* vol. VII (Eyring, H., ed.), Academic, New York, pp. 675–698.
77. Walton, A. G. (1969) Nucleation in liquids and solutions, in *Nucleation* (Zettlemoyer, A. C., ed.), Marcel Dekker, New York, pp. 225–307.
78. Chernov, A. A. and Komatsu, H. (1995) Principles of crystal growth in protein crystallization, in *Science and Technology of Crystal Growth* (van der Eerden, J. P. and Bruinsma, O. S. L., eds.), Kluwer Academic, Dordrecht, The Netherlands, pp. 329–353.
- 79 Gilmer, G. H., Ghez, R., and Cabrera, N. (1971) An analysis of combined volume and surface diffusion processes in crystal growth. *J. Crystal Growth* **8**, 79–93.
80. van der Eerden, J. P. (1994) Crystal growth mechanisms, in *Handbook of Crystal Growth* vol. 1a (Hurle, D., ed.), North Holland, Amsterdam, pp. 307–476.
81. De Yoreo, J. J. (2001) Eight years of AFM: what has it taught us about solution crystal growth, in *Thirteenth International Conference on Crystal Growth* (Hibiya, T., Mullin, J. B., and Uwaha, M., eds.), Elsevier, Kyoto, Japan.
- 82 Petsev, D. N. and Vekilov, P. G. (2000) Evidence for non-DLVO hydration interactions in solutions of the protein apoferritin. *Phys. Rev. Lett.* **84**, 1339–1342.
- 83 Israelachvili, J. and Pashley, R. (1982) The hydrophobic interaction is long range decaying exponentially with distance. *Nature* **300**, 341,342.
- 84 Israelachvili, J. and Wennerstrom, H. (1996) Role of hydration and water structure in biological and colloidal interactions. *Nature* **379**, 219–225.
- 85 von Smoluchowski, M. (1918) Versuch einer matematischen theorie der koagulationskine. *Z. Phys. Chem.* **92**, 129–135.
86. Zeldovich, J. B. (1942) On the theory of formation of new phases: cavitation. *J. Theor. Exp. Phys. (USSR)* **12**, 525–538.
87. Zwanzig, R. (2001) *Nonequilibrium Statistical Mechanics*, Oxford University Press, Oxford, UK.
- 88 Frenkel, J. (1932) *Phys. J. USSR* **1**, 498–510.
89. Broughton, J. Q., Gilmer, G. H., and Jackson, K. A. (1982) Crystallization rates of a Lennard-Jones liquid. *Phys. Rev. Lett.* **49**, 1496–1500.
- 90 Garcia-Ruiz, J. M. and Moreno, A. (1997) Growth kinetics of protein single crystals in the gel acupuncture technique. *J. Crystal Growth* **178**, 393–401.
- 91 Hou, W. B., Kudryavtsev, A. B., Bray, T. L., DeLucas, L. J., and Wilson, W. W. (2001) Real time evolution of concentration distribution around tetragonal lysozyme crystal: case study in gel and free solution. *J. Crystal Growth* **232**, 265–272.
- 92 Malkin, A. J., Kuznetsov, Y. G., Glanz, W., and McPherson, A. (1996) Atomic force microscopy studies of surface morphology and growth kinetics of thaumatin crystallization. *J. Phys. Chem.* **100**, 11,736–11,743.
- 93 Vekilov, P. G., Thomas, B. R., and Rosenberger, F. (1998) Effects of convective solute and impurity transport on protein crystal growth. *J. Phys. Chem.* **102**, 5208–5216.
- 94 Vekilov, P. G., Kuznetsov, Y. G., and Chernov, A. A. (1992) Interstep interaction in solution growth; (101) ADP face. *J. Crystal Growth* **121**, 643–655.
95. Vekilov, P. G., Kuznetsov, Y. G., and Chernov, A. A. (1992) The effect of temperature on step motion: (101) ADP face. *J. Crystal Growth* **121**, 44–52.

96. Borchers, H., ed. (1955) Landoldt-Bornstein numerical data and functional relationships, in *Materials Values and Mechanical Behaviour of Nonmetals*, vol. IV, pt. II, Springer, Berlin.
97. Bauser, E. (1994) Atomic mechanisms in semiconductor liquid phase epitaxy, in *Handbook of Crystal Growth*, vol. 3b (Hurle, D. T. J., ed.), North Holland, Amsterdam, pp. 879–911.
98. Ehrlich, G. and Hudda, F. G. (1966) Asymmetric capture at steps. *J. Chem. Phys.* **44**, 1039–1052.
99. Braun, N., Tack, J., Fischer, M., Bacher, A., Bachmann, L., and Weinkauff, S. (2000) Electron microscopic observations on protein crystallization: adsorption layers, aggregates and crystal defects. *J. Crystal Growth* **212**, 270–282.
100. Bostanov, V., Staikov, G., and Roe, D. K. (1975) Rate of propagation of growth layers on cubic crystal faces in electrocrystallization of silver. *J. Electrochem. Soc.* **122**, 1301–1305.
101. Vekilov, P. G., Monaco, L. A., and Rosenberger, F. (1995) Facet morphology response to non-uniformities in nutrient and impurity supply. I. Experiments and interpretation. *J. Crystal Growth* **156**, 267–278.
102. Lin, H., Petsev, D. N., Yau, S. T., Thomas, B. R., and Vekilov, P. G. (2001) Lower incorporation of impurities in ferritin crystals by suppression of convection: modeling results. *Crystal Growth Design* **1**, 73–79.
103. Reviakine, I., Georgiou, D. K., and Vekilov, P. G. (2003) Capillarity effects on the crystallization kinetics: insulin. *J. Am. Chem. Soc.* **125**, 11,684–11,693.
104. Malkin, A., Kuznetsov, Y., and McPherson, A. (1997) An in situ AFM investigation of catalase crystallization. *Surf. Sci.* **393**, 95–107.
105. Vekilov, P. G., Ataka, M., and Katsura, T. (1993) Laser Michelson interferometry investigation of protein crystal growth. *J. Crystal Growth* **130**, 317–320.
106. Vekilov, P. G. and Rosenberger, F. (1996) Dependence of lysozyme growth kinetics on step sources and impurities. *J. Crystal Growth* **158**, 540–551.
107. Kuznetsov, Y. G., Konnert, J., Malkin, A. J., and McPherson, A. (1999) The advancement and structure of growth steps on thaumatin crystals visualized by atomic force microscopy at molecular resolution. *Surf. Sci.* **440**, 69–80.
108. Vekilov, P. G. and Chernov, A. A. (2002) The physics of protein crystallization, in *Solid State Physics* vol. 57 (Ehrenreich, H. and Spaepen, F., eds.), Academic, New York, pp. 1–147.
109. Bennema, P. (1967) Analysis of crystal growth models for slightly supersaturated solutions. *J. Crystal Growth* **1**, 278–286.